Nickel substitution induced reentrant spin glass behavior in $EuGa_4$

Ashutosh Kumar Singh,[1,2] Debendra Prasad Panda,[1,2] Sakshi Mehta,[3] Abhishake Mondal,[3] and Sebastian C. Peter[2,4,*]

[1]*Chemistry and Physics of Materials Unit, Jawaharlal Nehru Centre for Advanced Scientific Research (JNCASR), Bangalore 560 064, India*

[2]*School of Advanced Materials, JNCASR, Bangalore 560 064, India*

[3]*Solid State and Structural Chemistry Unit, Indian Institute of Science (IISc), Sir C V Raman Road, Bangalore 560012, India*

[4]*New Chemistry Unit, JNCASR, Bangalore 560 064, India*

(Received 7 August 2022; revised 30 October 2022; accepted 29 November 2022; published 16 December 2022)

Typically, atomic scale disorder is essential to show glassy behavior and amorphous materials can be the optimum candidates in this regard. Generating local disorder in an ordered material by substitution of another metal is a challenging task. In this paper, we successfully substituted Ni in $EuGa_4$ ($EuNi_{0.37}Ga_{3.63}$) to induce spin glass (SG) behavior. The compound was characterized by single-crystal x-ray diffraction, dc magnetization, frequency-dependent ac susceptibility, isothermal magnetization at various temperatures, spin relaxation, specific heat, and electric resistivity. Two distinct anomalies were observed in dc susceptibility $\sim$ 16.5 and 5.2 K corresponding to long-range antiferromagnetic (AFM) ordering and SG transition, respectively. Their characteristic peaks in specific heat capacity further support the AFM and SG behavior. The irreversibility temperature is fitted with the Almeida-Thouless equation, confirming the Ising SG. The SG behavior is further confirmed by shift of maxima to a high temperature in ac susceptibility with increasing frequency. Nonzero spin relaxation after 7200 s, fitted with stretched exponential model, provides the value of $\beta = 0.41$. This material can be identified as a possible reentrant SG as AFM and SG behavior coexist in the low-temperature range. Additionally, a spin-flip transition is observed in the AFM region (5.2 K $< T <$ 16.5 K). Our first-principles calculations show Ni substitution induces the distortion in electronic band structure as compared with parent $EuGa_4$. A minimal difference between the different magnetic configurations for Ni-substituted $EuGa_4$ suggests the frustration in the lattice, pointing toward SG behavior.

DOI: 10.1103/PhysRevB.106.224414

I. INTRODUCTION

Spin glass (SG) is a phenomenon of disordered spins in the crystal lattice, which shows a classical phase transition at a critical temperature. However, SG differs from the ferromagnetism (FM) and antiferromagnetism (AFM) owing to the lack of long-range magnetic ordering. Generally, SG in a material is observed due to disorder and frustration, which leads to competition in AFM and FM interaction [1–3]. In some cases, dynamic frustration can also lead to SG behavior [4]. Although SG behavior was initially observed in AuFe solid solution [5], later, rare-earth (RE)-based intermetallics have gained more attention due to the strong correlated electrons and the presence of the crystal electric field, which play important roles in observation of SG behavior [1]. Several RE-based intermetallics have been reported for SG [6–9]. They are also known for complex magnetic behavior, such as multiple magnetic transitions [10–13] and charge density wave (CDW) [14–19]. The presence of long- and short-range magnetic ordering increases the complexity, for example, with the FM-to-SG transition in $Cr_{75}Fe_{25}$ [20] and $Ni_2Mn_{1.36}Sn_{0.64}$ [21]. A material which exhibits the transition from long- to short-range order upon lowering the temperature is known as reentrant SG (RSG). The classic example of RSG is $Eu_xSr_{1-x}S$ [22], which is proposed by the Sherrington-Kirkpatrick (SK) model theoretically [23].

The $RETX_3$ (T = transition metals, $X = p-$block elements) series of compounds are rich in structure and magnetic properties [24–27]. In this class of intermetallic, mainly Pr-based intermetallics (crystallizes in $BaNiSn_3$-type noncentrosymmetric crystal structure) are known to exhibit SG behavior [28,29], along with $GdCuGa_3$ [30] and $CeRuGe_3$ [31]. SG behavior in Pr-based intermetallics is interesting due to the lack of frustration and disorder of the system, understood as dynamic frustration [4]. In contrast, the SG property in $GdCuGa_3$ and $CeRuGe_3$ is believed to originate from spin-reorientation Gd^{3+} [30] and nonmagnetic atom disorder (Ge disorder at 24k Wyckoff position), respectively. Furthermore, $EuTGe_3$ (T = Co, Ni, Rh, Pd, and Ir) compounds crystallizing in the $BaNiSn_3$-type structure have been reported for the AFM (T_N = 10–17 K) ground state [32,33]. Among them, $EuTX_3$ (T = Co, Ni, and Ir) show multiple magnetic transitions. The magnetic structure of $EuNiGe_3$ determined by neutron diffraction reveals the equal-moment helicoidal structure with an incommensurate wave vector (k = 1/4 d 0) [34]. In $EuNiGe_3$, the paramagnetic (PM)-to-AFM phase transition is mediated by the incommensurately modulated phase (collinear) determined by Mössbauer spectroscopy [35].

The $BaAl_4$ structure type has recently gained much attention due to its nontrivial band topology. A binary intermetallic $EuGa_4$ crystallizing in the centrosymmetric $BaAl_4$ structure

*sebastiancp@jncasr.ac.in

type with $I4/mmm$ space group hosts the AFM ground state [36]. The EuX_4 (X = Ga, Al) compounds show giant magnetoresistance [37], topological Hall effect [37,38], and CDW ($EuGa_4$ shows > 1 GPa) [16–18,39]. The neutron diffraction and μSR study on $EuGa_4$ shows the A-type AFM magnetic structure [40,41]. However, the physical properties of these materials can be altered by substitution or doping. The $BaAl_4$ lattice has three atomic positions, one for Ba and two for Al atoms. Substitution at different atomic positions has led to change in magnetic properties. For example, AFM transition temperature T_N decreases from 16.5 to 13 K by substitution of Yb at the Eu site in $EuGa_4$ [36,42]. A similar lowering of the AFM transition occurs upon Li and Mg substitution at the Ga atomic position [43]. Additionally, the magnetic ordering changed to FM upon Si substitution at the Al position in $EuAl_4$ [44].

Several compounds with a general formula of $EuTGa_3$ crystal were grown, but none crystallized in the $BaAl_4$-structure type. However, Li and Mg atoms substituted at the Ga site in nonstoichiometric amounts retain the crystal structure [43]. It indicates the robustness of the polar intermetallic structure and resistance toward any foreign element, as Bobev *et al.* [36] indicated in their attempt to replace Ga atoms with Si and Sn atoms. Here, in this paper, we have substituted Ni atoms at the Ga site with a nominal composition of $EuNi_{0.37}Ga_{3.63}$. In contrast to the previous report, substitution in the lattice induces more complex SG behavior $<\sim 5.2$ K while retaining the unchanged AFM transition in $EuGa_4$ and classifying it as a possible RSG. A detailed magnetic susceptibility (dc and ac), magnetic relaxation, thermodynamic, electric, and first-principles calculations were performed to study the SG behavior.

II. EXPERIMENTAL DETAILS

Eu, Ni, and Ga metals were taken in the ratio of 1:1:10 in an alumina crucible. The weighing of the metals was done in the Argon-filled glove box and later sealed in an evacuated quartz ampoule. The ampoule was slowly heated to 1000 °C in 24 h, kept for 24 h, and cooled down to 500 °C at a rate of 2 °C/h. The ampoule was decanted and centrifugated at that temperature to remove the excess Ga flux. Any residue Ga flux was cleaned using dimethylformamide and I_2 solution by sonication. The shiny silver crystals obtained are cylindrical shaped. The handpicked single crystals were used for single-crystal x-ray diffraction (SCXRD) studies. The single-crystal data were collected on a Bruker APEX3 diffractometer using Mo-$K\alpha$ radiation ($\lambda = 0.71073$ Å) at 300 K. The structures were solved with the SHELXS structure solution program using direct methods and refined with the SHELXL refinement package using least squares minimization [45]. The structure was solved in the $I4/mmm$ space group with mixed occupancy of Ni at the Ga2 position. The structure was refined until the R factor and goodness of fit attained values of 3.17 and 1.077, respectively. Crystallographic data are listed in Table SI in the Supplemental Material [46].

The composition and color mapping analyses were done using scanning electron microscopy (SEM)-energy-dispersive x-ray spectroscopy (EDS) on the Leica instrument. The color mapping shows the uniform distribution of all the elements. The phase purity of the bulk sample was determined using powder x-ray diffraction (XRD). Data were collected using Rigaku miniflex x-ray diffractometer with Cu−K_α as the x-ray source ($\lambda = 1.5406$ Å). No other phase was found within the detection limit (< 2%) of powder XRD. A selected area diffraction pattern (SAED) was collected using JEOL 200 KeV transmission electron microscopy (TEM) to confirm phase purity further.

The magnetic measurements were carried out with a Quantum Design Magnetic Property Measurement System, Superconducting Quantum Interference Device (MPMS-SQUID) dc. Temperature-dependent magnetization data were collected in the field-cooled (FC) and zero-FC (ZFC) modes in a temperature range of 2–300 K with a varying magnetic field. Isothermal magnetizations were done at various temperatures in the magnetic field of −7 to 7 T. Heat capacity was measured in relaxation mode, and transport properties were measured by a four-probe connection using the Physical Property Measurement System (PPMS, Quantum Design).

We implemented the first-principles calculations based on density functional theory (DFT) embedded in the QUANTUM ESPRESSO code [47]. The generalized gradient approximation exchange-correlation energy functional used for these calculations are parametrized by Perdew, Burke, and Ernzerhof [48]. The projector augmented-wave function was used [49]. Electronic wave functions and charge density were represented in a plane-wave basis set truncated with cutoff energy of 45 and 400 Ry, respectively. The integration over the Brillouin zone was sampled with a dense 10 × 10 × 5 mesh of k points.

III. RESULTS AND DISCUSSION

$EuNi_{0.37}Ga_{3.63}$ crystallizes in body-centered tetragonal space group $I4/mmm$ [Fig. 1(a)], determined by SCXRD, powder XRD, and SAED. The lattice parameters determined using SCXRD are $a = b = 4.4015(2)$ Å and $c = 10.6781(7)$ Å, in close agreement with parent $EuGa_4$ [36]. The a and b lattice parameters decrease, while the c lattice parameter increases marginally. All the relevant crystallographic data are provided in Tables SI–SIII in the Supplemental Material [46]. The SCXRD raw data integration gives the mean $|E^2-1|$ statistic of 0.766, which is close to the noncentrosymmetric crystal system ($|E^2-1| = 0.73$ for noncentrosymmetric and 0.98 for centrosymmetric). However, the structure solution in $I4mm$ results as nonpositive definite (NPD), indicating the wrong structure model for the structure refinement. Subsequently, data were solved in the centrosymmetric space group $I4/mmm$ and refined. The structure was refined in the $I4/mmm$ space group, containing the 2a Wyckoff position for Eu atoms and 4d and 4e for Ga atoms. It is reported in the literature that mostly dopants are substituted in the 4d position [17,43,50,51], separated by the 4e Ga atoms forming square pyramidal geometry. However, to find the best-suited structure model, we mixed the Ni with Ga atoms at 4d and 4e Wyckoff positions in separate refinements. Both refinements give a satisfactory structure solution. The anisotropic displacement parameter (ADP) was used to determine the correct atomic position of Ni. The lower ADP value was conclusive for Ni atoms to occupy the 4e Wyckoff position. In a theoretical study on site occupancies

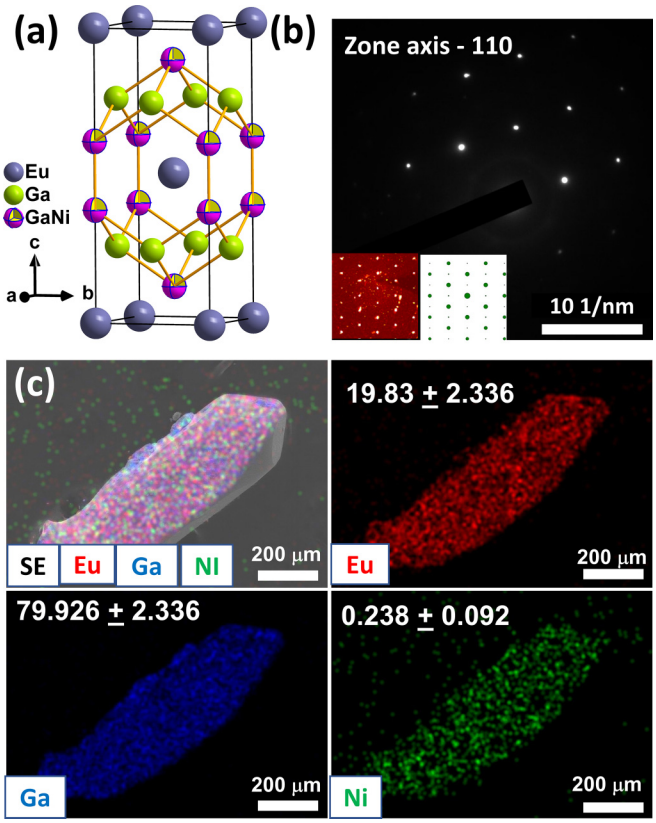

FIG. 1. Structure characterization of $EuNi_{0.37}Ga_{3.63}$. (a) The unit cell of $EuNi_{0.37}Ga_{3.63}$, where Ni atoms are mixed at 4*e* Wyckoff with Ga atoms. (b) The selected area diffraction pattern (SAED)-transmission electron microscopy (TEM) image along the zone axis 110 matches closely with the simulated SAED pattern from single-crystal x-ray diffraction (SCXRD) and PTCLab software. (c) The scanning electron microscopy (SEM)-energy-dispersive x-ray spectroscopy (EDS) color mapping shows a representative single crystal and uniform distribution of Eu, Ni, and Ga. The corresponding atomic percentage is written for each element.

of the dopant in the $BaAl_4$ structure type, Häussermann *et al.* [52] state that elements with higher electronegativity (EN) occupy the 4*e* Wyckoff position (EN of Ni = 1.91, EN of Ga = 1.81 on the Pauling scale), which further supports our SCXRD determined site occupancies. The SAED pattern [Fig. (1b)] was collected at room temperature (300 K) along the 110 zone axis, which corroborates with simulated SCXRD and PTCLab [inset of Fig. 1(b)] [53], confirming the centrosymmetric space group of this compound. The SEM-EDS mapping shows uniform elemental distribution, but the Ni concentration is lower than the expected ∼ 9 at. %, Fig. 1(c). It can be attributed to the relative *K*-edge values for Ni and Ga, where a broad Ga peak hinders determining the true atomic concentration of Ni.

All dc magnetic measurements were done on the polycrystalline sample. The ZFC and FC susceptibility measurements at the various magnetic fields as a function of temperature are presented in Fig. 2(a). The magnetic susceptibility at 0.1 T of the applied magnetic field shows the two magnetic anomalies at 16.5 and 5.2 K in ZFC and FC modes. The different bifurcation behavior in ZFC and FC curves below anomaly temperature indicates a different type of magnetic transition. The overlap of ZFC and FC curves until 16.53 K and λ-shaped transition in specific heat data confirm the AFM transition (T_N), which is in close agreement with previous reports [36,37,41]. The bifurcation in ZFC and FC curves is a preliminary indicator of SG behavior. The nature of bifurcation in dc magnetic susceptibility is probed with a dissimilitude magnetic field (0.005–0.5 T). The cusplike behavior (∼ 16.5 K) is retained until the highest applied magnetic field without any shift in temperature. In contrast, the cusplike behavior at 5.2 K shifts toward lower temperature and vanishes out on the high magnetic field (0.5 T), confirming the short-range ordering, Fig. 2(a). The Curie-Weiss fit in the temperature range of 220–300 K results in the effective PM moment (μ_{eff}) of 6.98 μ_B/f.u., which is in close agreement with the DFT-calculated magnetic moment of 6.73 μ_B/f.u. However, it is considerably less than the theoretical magnetic moment of Eu^{2+} of 7.93 μ_B, Fig. 2(b). The lower value of μ_{eff} can be explained by two factors: (1) crystalline electric field and (2) change in the valence state of Eu^{2+} to Eu^{3+} [54–57]. The Curie-Weiss temperature of −98.8 K shows the dominant AFM interaction. The magnetic frustration defined as $f = |\theta_{CW}|/T_N = 5.85$ indicates a moderately frustrated system [58,59]. The bifurcation in the ZFC and FC curves (defined as T_{irr}) decreases upon an increase in the magnetic field, confirming short-range ordering in the system, as shown in Figs. 2(c)–2(e).

The magnetic field dependence of T_{irr} is used to characterize Ising SG, using the Almeida-Thouless (AT) line [60]. The AT line represents the SG phase boundary separating from the PM region. According to mean-field theory, the AT line is represented as

$$T_{irr}(H) = T_{irr}(0)(1 - CH^n),$$

where T_{irr} (0) is the bifurcation temperature for zero magnetic fields, *C* is constant, and *n* has a theoretical value of 2/3 for Ising SG [3]. Figure 2(g) shows the experimental data best fitting with the AT line. The fitting parameter obtained at T_{irr} (0) is 5.655 (9) K, and *n* is 0.653 (1), which is in complete agreement with Ising SG of 0.66. The isothermal magnetization at different temperatures is shown in Fig. 2(h). The $M(H)$ curve at 300 K shows a typical PM nature of the sample, while at 25 K, an S-like shape is observed. At 10 and 7 K, the magnetic moment does not saturate until the highest applied magnetic field (7 T); however, a slope change is observed. The change in slope of magnetization under the applied magnetic field can be associated with the reorientation of spin [metamagnetic transition (MMT)]. A slope change is observed at 0.34 and 6.27 T and 0.15 and 5.72 T for 7 and 10 K isotherms, respectively. However, slope change is small compared with the high magnetic field spin-flip transition. A similar kind of MMT is observed in Al-substituted $EuGa_4$ but absent in parent $EuGa_4$ [17,39], which shows the A-type AFM [41]. The observed MMT in the present sample can be attributed to the magnetocrystalline anisotropy, spin-canting, and magnetic exchange interactions due to varying Ruderman-Kittel-Kasuya-Yosida interaction, which originate from Ni substitution in the lattice [61]. Surprisingly, the MMT point increases with a decrease in temperature, indicating the canted AFM behavior in Ni-substituted $EuGa_4$ [17,62].

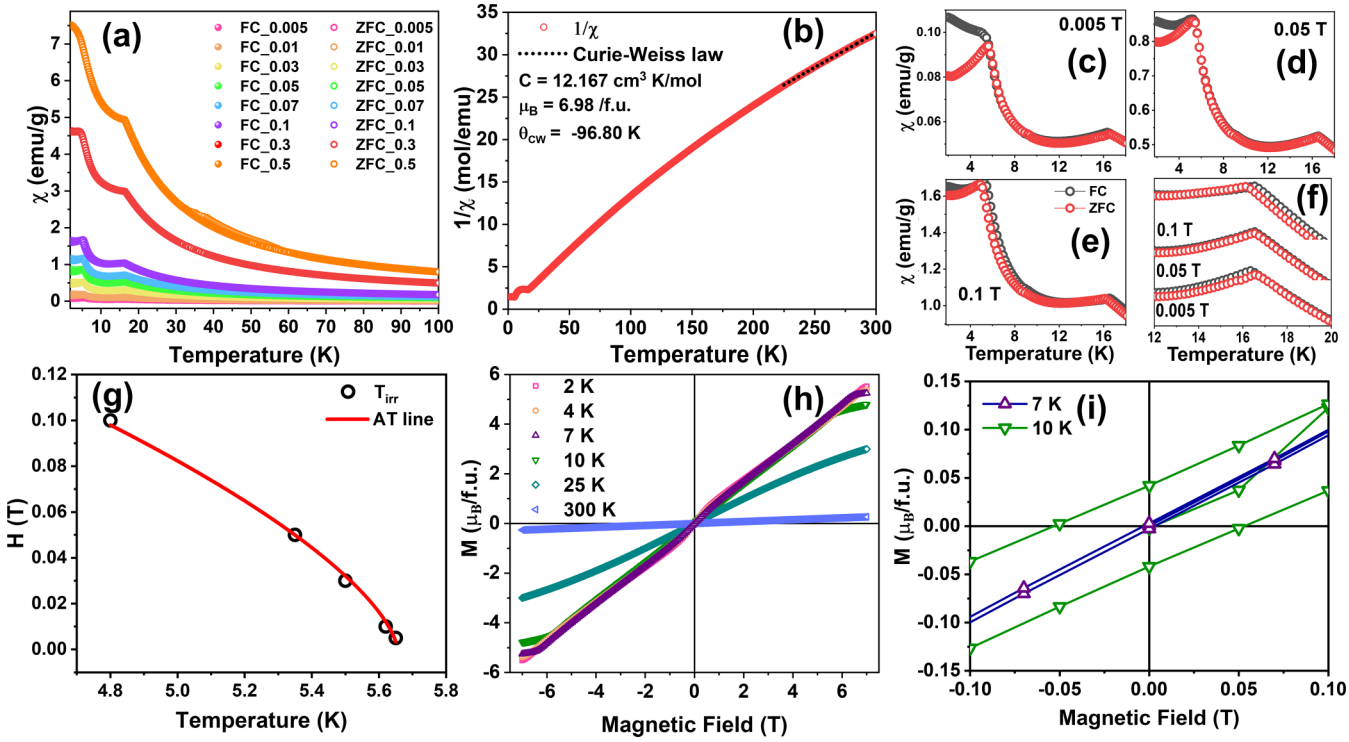

FIG. 2. dc magnetic measurement on a polycrystalline sample of the crushed single crystals. (a) Zero-field-cooled (ZFC) and field-cooled (FC) magnetic susceptibility data with various applied magnetic fields. (b) The FC inverse susceptibility at 0.1 T fitted with the Curie-Weiss law in the linear temperature range of 225–300 K. (c)–(e) Bifurcation in ZFC and FC curve < 5.5 K. With an increasing magnetic field, it ceases. (f) The antiferromagnetic (AFM) transition ~ 16.53 K does not shift with an increased magnetic field. (g) Fitting of spin freezing temperature with Almeida-Thouless (AT) line, data best fitted for $n = 0.653$ (1), in agreement with Ising spin glass behavior ($n = 0.66$). (h) Isothermal magnetization (ITM) curve against varying magnetic fields at different temperatures. (i) Presence and absence of hysteresis at 10 and 7 K, respectively.

An AFM state < 16.5 K and SG behavior < 5.2 K prompt us to look for RSG behavior. RSG behavior is defined as a system having a high-temperature long-range ordering (FM/AFM) and a subsequent cooling leading to SG behavior with the destruction of long-range ordering [58,63]. In the M vs H data, a hysteresis at 10 K (~ 0.05 T), Fig. 2(i), the magnetic field induced spin-flip transition ~ 5.64 T, and a nonsaturating magnetic moment at the highest applied magnetic field confirm the AFM state in the temperature range of $5.2\ \text{K} < T(\text{K}) < 16.5$ K. In the M vs H curve < 5.2 K, the absence of hysteresis and magnetic field induced transition along with nonsaturating magnetic moment confirms SG behavior upon the destruction of the AFM state. An essential characteristic of SG behavior is its different behavior after removing the magnetic field. Since SG is a nonequilibrium state of the matter, theoretically, upon removing the magnetic field, the SG state decays its magnetic moment in infinite time. The following protocol mapped SG behavior using thermoremanent magnetization (TRM).

The sample was cooled down to 2 K under the applied magnetic field of 0.01 T and kept there for 1 min, followed by the magnetic field being switched off, and the magnetic moment was recorded as a function of time (until 7200 s). The measured TRM data against the time on a logarithmic scale are presented in Fig. 3. The M_{TRM} decays slowly over time and remains nonzero even after 2 h of decay (in fact, it decays only $\sim 4\%$), which is a clear signature of SG behavior.

The nature of decays can be better understood by fitting the different relaxation mechanisms. There are three different decay mechanisms that have been proposed: (1) power law, (2) logarithmic decay, and (3) modified-stretched fractional exponential decay (MSFED) [3,64]:

$$M_{\text{TRM}}(t) = M_0 t^{-\gamma}, \quad \text{power law}, \tag{1}$$

$$M_{\text{TRM}}(t) = m_0 - S\ln(t), \quad \text{logarithmic decay}, \tag{2}$$

$$M_{\text{TRM}}(t) = m_0 - m_g \exp\left[-\left(\frac{t}{\tau}\right)^{\beta}\right], \quad \text{MSFED}. \tag{3}$$

The power law in Eq. (1) describes the relaxation mechanism in a long-range ordered system such as AFM and FM but failed in most system. However, Monte Carlo simulations were successfully used in some SG systems (using the Ising model) [65]. In contrast, Eq. (2) is widely used for the system containing the uniform barrier over which magnetic relaxation takes place (from zero to a maximum value) [3,66]. However, a lousy fitting is obtained using Eqs. (1) and (2), Fig. 3(a).

Equation (3) results in the best fitting, where m_0 is initial magnetization, m_g is a contribution from the SG component, τ is the time constant, and β is the stretching component (relaxation rate). All the fitting parameters are listed in Table SIV in the Supplemental Material [46]. Here, β is the most important parameter to look for, representing the energy

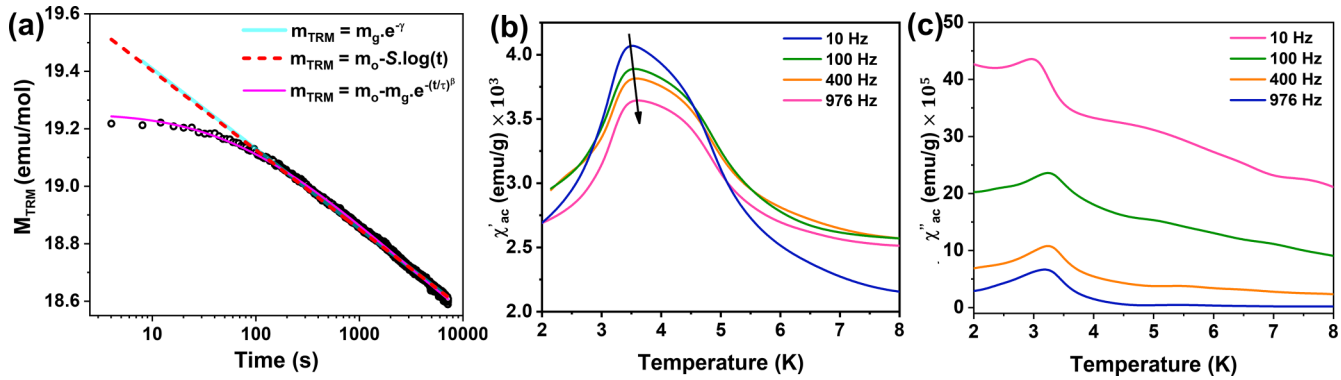

FIG. 3. Spin glass dynamic study with time and frequency dependence. (a) Time dependence of thermoremanent magnetization (TRM) at 2 K. Different relaxation mechanisms have been used for fitting the raw data. The best fit was obtained using the modified-stretched fractional exponential decay (MSFED) model. The power law and logarithmic decay model deviate during the initial spin-relaxation process. (b) Variation of real part of ac susceptibility with increase in frequency to high temperature. (c) The imaginary part of ac susceptibility does not vary with frequency after 100 Hz.

barrier in the system. A β value of 0 indicates no relaxation, and $M_{\mathrm{TRM}}(t)$ remains constant, while a β value of 1 indicates uniform relaxation with a single time constant. An intermediate value of $0 < \beta < 1$ confirms the multitude of energy barriers present.

The MSFED fitting results of the β value of 0.41 confirms the SG ground state in the system [1]. The mean relaxation time $\tau = 2214$ s is comparable with the best-known SG system [28,29,67,68]. To probe the origin of SG behavior, a model developed by Ulrich *et al.* [69] has been employed. After a crossover time, the negative logarithmic rate of change of magnetic moment $\{w(t) = -\frac{\mathrm{d}}{\mathrm{d}t}[\ln m(t)]\}$ decays with time as a power law $W(t) = At^{-n}$. However, a plot of $w(t)$ against time does not correspond to available literature and is a poor fit with the power law. Thus, the nature of SG, cluster SG, or canonical SG cannot be determined from the M_{TRM} data.

Spin dynamics of the compounds are further investigated using the temperature- and frequency-dependent ac susceptibility. The real and imaginary parts of ac magnetic susceptibility are shown in Figs. 3(b) and 3(c), respectively. In the real part of ac magnetic susceptibility (χ'_{ac}), a peak at ~ 3.63 K at 10 Hz is observed, which moves toward higher temperatures with an increase in applied frequency, confirming SG behavior. The falling shape of χ'_{ac} below spin freezing temperature is the characteristic nature of RSG behavior [61,70]. However, maxima vary by 0.06 K in the 11–976 Hz frequency range, Fig. 3(b). A frequency-dependent maximum fitting in ac susceptibility using the Mydosh parameter (S) has been used for characterizing SG, where $S = \frac{\Delta T_f}{T_f \Delta \log(\nu)}$. For canonical SG, the value of S is in the range of 0.0045–0.02 [71]. A partial change in frequency-dependent χ'_{ac} hints at noncanonical SG behavior. The imaginary part of ac magnetic susceptibility (χ'') shows the maxima at 3.03 K (at 10 Hz), shifts to 3.25 for 100 Hz, and remains constant upon further increased frequency [Fig. 3(c)]. Similar ac magnetic susceptibility behavior is observed in $PrRuSi_3$ [29].

The specific-heat measurement was performed in PPMS by a modified heat-pulse method in the temperature range of 2–50 K. The specific heat C_p vs T is plotted in Fig. 4. First, there are two anomalies: a long-range ordering characteristic

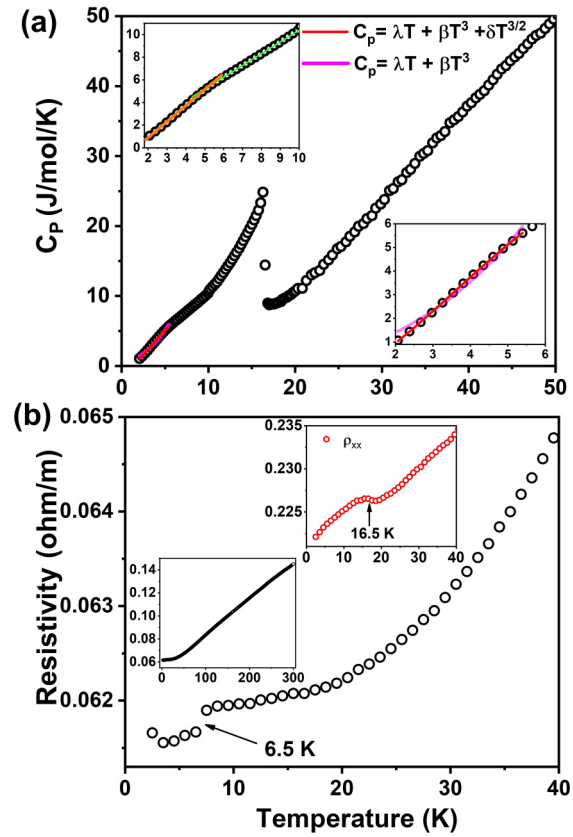

FIG. 4. Thermodynamic and transport measurement on $EuNi_{0.37}Ga_{3.63}$. (a) Temperature-dependent specific heat of the sample $EuNi_{0.37}Ga_{3.63}$. A long-range ordering at 16.5 K is inferred as an antiferromagnetic (AFM) transition. The low-temperature part 2–10 K is shown in the upper left corner, confirming the broad hump; the orange and green line is used to show the point of intersection at 5.2 K. Specific heat data in the glassy region are fitted with two equations, and the best fit was obtained upon addition of magnetic term. (b) Electrical resistivity (ρ) // and $\perp$ to c axis. Metallic behavior in the temperature range of 2–300 K (lower inset). Signature of AFM transition at 16.5 K $\rho//c$ is observed (upper inset).

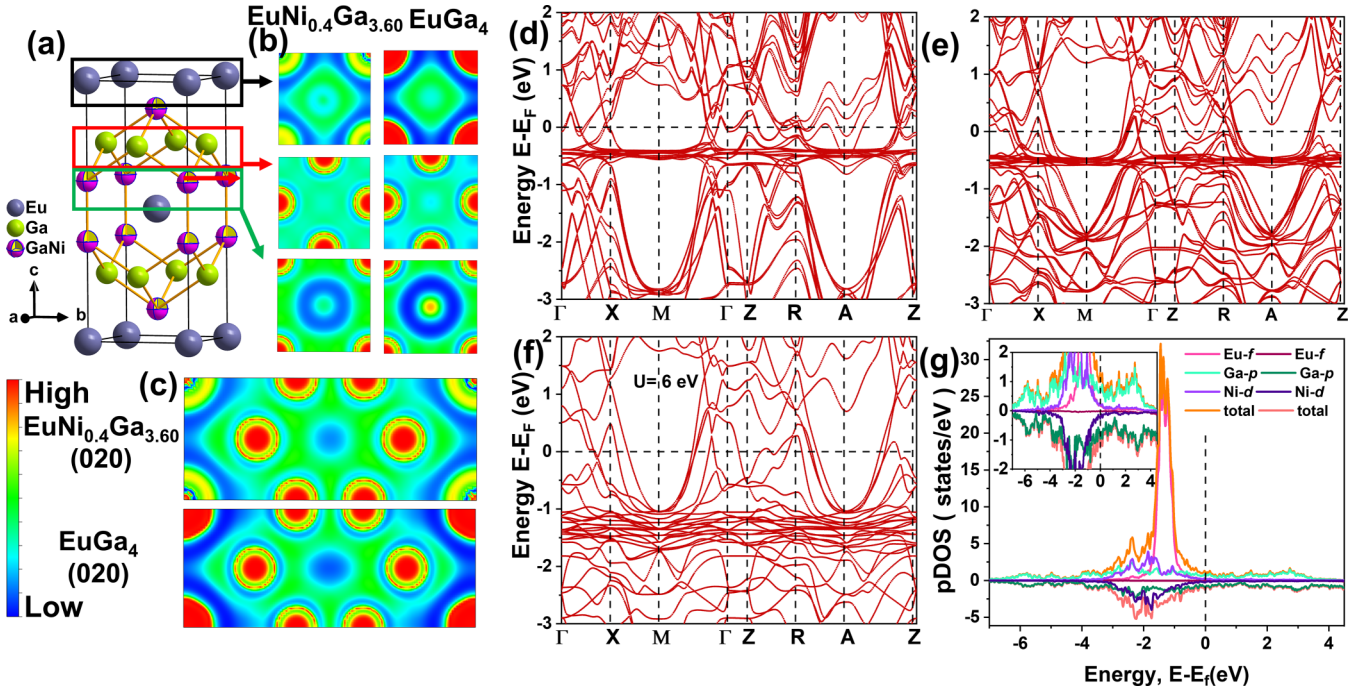

FIG. 5. Density functional theory (DFT) calculation for Ni-substituted $EuGa_4$. Electron localization function (ELF) analysis for Ni-substituted $EuGa_4$ and $EuGa_4$ to understand electronic density distribution in a different plane. (a) The crystal structure of $EuNi_{0.37}Ga_{3.63}$ is marked with different planes. (b) Corresponding to plane in (a) electronic density compared with $EuGa_4$. (c) Comparison of 020 planes. (d) Electronic band structure calculation for $EuGa_4$ without onsite Hubbard potential. (e) The electronic band structure for Ni-substituted $EuGa_4$ ($EuNi_{0.40}Ga_{3.60}$) induces several additional electronic bands. (f) Effect of onsite Hubbard potential of $U = 6$ eV, scatter the electronic bands. (g) The partial density of states (pDOS) plot for Ni-substituted $EuGa_4$, an overlap of Eu-f, Ga-p, and Ni-d orbitals confirming the bonding of Eu, Ni, and Ga atoms.

λ peak at 16.5 K (AFM) and one broad hump ∼ 5 K. The frozen spin below the expected temperature results in a broad hump Fig. 4 (inset top left), along with dc-ac susceptibility and TRM, confirming SG behavior. Specific heat data are fitted in the temperature range of 2–5.5 K. Two fitting models were used:

$$C_P = \lambda T + \beta T^3, \tag{4}$$

$$C_P = \lambda T + \beta T^3 + \delta T^{3/2}. \tag{5}$$

However, the best fitting was obtained upon adding a magnetic term, Fig. 4(a) (inset bottom right). Since we have ruled out any possibility of long-range magnetic ordering at low temperature, the additional magnetic term confirms the presence of short-range magnetic ordering. Temperature-dependent resistivity was measured using PPMS on single crystals in the temperature range of 2–50 K, Fig. 4(b).

Resistivity was measured using the standard four-probe method using the Cu wire electrode. It shows metallic behavior in the entire temperature range of 2–300 K in $\rho \perp c$ and linear behavior in the temperature range of 50–300 K. Saturating behavior is observed < 20 K and a dip at 6.5 K, closer to observed SG behavior. The ρ // c shows anomalies at 16.5 K, originating from the ordering of spins in AFM fashion, increasing resistivity. This anisotropic behavior in transport properties is expected, as the c/a ratio is ∼ 2.4.

DFT calculations were done using QUANTUM ESPRESSO [47]. The electron localization function (ELF) is used for understanding the bonding nature of constituent elements of a crystal lattice. Its value varies between 0 and 1, where 0 indicates the negligible probability of finding an electron in the vicinity, while 1 indicates 100% probability. The intermediate value of 0.5 indicates the shared electron density and covalent nature. Electronically, Ni substitution to the $EuGa_4$ lattice is understood by a comparative ELF plot [Figs. 5(a)–5(c)]. A decrease in ELF density is observed near corresponding nuclei, increasing the covalent character compared with polar $EuGa_4$ [36]. The calculated electronic band structure and partial density of states (pDOS) are shown in Fig. 5. The electronic band structure for $EuGa_4$ is shown in Fig. 5(d). Several bands crossing the Fermi level confirm the metallic nature [36]. Ni substitution in the $EuGa_4$ lattice retains the metallic property observed in our resistivity measurement. However, contrary to $EuGa_4$, several bands are generated along the high-symmetry line X-M-Γ and R-A-Z in Ni-substituted $EuGa_4$. These additional bands originate from the Ni hybridization of Ga and Eu atoms, as confirmed from pDOS calculations, Fig. 5(e). The onsite Hubbard potential of $U = 6$ eV was applied on the Eu atom, showing the Eu f orbital moves away from the Fermi line, Fig. 5(f). Total energy was calculated in different magnetic structures to get the ground state of the Ni-substituted $EuGa_4$. The $EuGa_4$ magnetic structure is taken as the starting model [36]. Three magnetic configurations were prepared by incorporating the Ni magnetic moment in the system. The total energy for all three magnetic configurations

is shown in Table SV in the Supplemental Material [46]. The negligible energy difference between all magnetic configurations in Ni-substituted $EuGa_4$ suggests competition between FM and AFM ground states, which may lead to SG behavior in the system. To validate these claims, the total energy of $EuGa_4$ in AFM and FM states were calculated. The AFM state is more stable than the FM state by 92 meV and follows the measured A-type AFM structure [41]. A similar study was performed on Mn_2PtGa and $EuTe_2$ [72,73].

IV. CONCLUSIONS

In conclusion, we have successfully substituted Ni in a very stable $EuGa_4$, a body-centered tetragonal lattice, to generate local disorder and SG behavior. Crystal structure and magnetic and transport properties were studied in detail, and bifurcation in ZFC and FC susceptibility < 5.4 K hints at SG behavior. SG behavior is further confirmed by thermoremanent magnetization and ac susceptibility. Relaxation behavior is best explained using the MSFED method. The thermoremanent magnetization experiment in SG relaxes with a high relaxation time $\tau = 2214$ s. A minute high-temperature shift of ac susceptibility with frequency confirms the noncanonical SG nature. The presence of the AFM transition at 16.5 K, which disappears at SG freezing temperature < 5.2 K, leads us to classify this material as a possible RSG, which warrants additional experiments. It shows metallic behavior with significant anisotropy. However, there are very few theoretical attempts to understand noncanonical SG. One such theoretical model is a scale-free network, where SG can be generated solely in an AFM lattice with randomness [74,75]. Alteration of band structure and electronic density distribution is further confirmed by ELF analysis and band structure calculations.

ACKNOWLEDGMENTS

We thank JNCASR and Department of Science and Technology (DST), India, for financial support. A.K.S. thanks JNCASR for the research fellowship. D.P.P. thanks the Council of Scientific and Industrial Research for the research fellowship. A.M. and S.M. thank the Solid State and Structural Chemistry Unit at the IISc, Bangalore, India. S.C.P. thanks DST for the SwarnaJayanti Fellowship (No. DST/SJF/CSA-02/2017-18).

[1] J. A. Mydosh, Spin glasses: redux: An updated experimental/materials survey, Rep. Prog. Phys. **78**, 052501 (2015).
[2] J. A. Mydosh, Disordered magnetism and spin glasses, J. Magn. Magn. Mater. **157–158**, 606 (1996).
[3] C. Y. Huang, Some experimental aspects of spin glasses: A review, J. Magn. Magn. Mater. **51**, 1 (1985).
[4] E. A. Goremychkin, R. Osborn, B. D. Rainford, R. T. Macaluso, D. T. Adroja, and M. Koza, Spin-glass order induced by dynamic frustration, Nat. Phys. **4**, 766 (2008).
[5] V. Cannella and J. A. Mydosh, Magnetic ordering in gold-iron alloys, Phys. Rev. B **6**, 4220 (1972).
[6] S. Sarkar, S. Roy, D. Kalsi, and S. C. Peter, Ce_2PtGe_3: A new ordered orthorhombic superstructure in the AlB_2 family with spin glass behavior, Inorg. Chem. Front. **4**, 2097 (2017).
[7] D. X. Li, T. Yamamura, K. Yubuta, S. Nimori, Y. Haga, and T. Shikama, Evidence for spin-glass state in nonmagnetic atom disorder compound Pr_2AgIn_3, J. Phys. Conf. Ser. **320**, 012041 (2011).
[8] S. Rayaprol and R. Pöttgen, Gd_2Au_2Cd: A Mo_2FeB_2-type intermetallic with ferromagnetic ordering and spin glass anomalies, Phys. Rev. B **73**, 214403 (2006).
[9] D. X. Li, S. Nimori, Y. Shiokawa, A. Tobo, H. Onodera, Y. Haga, E. Yamamoto, and Y. Ōnuki, Spin-glass behavior with short-range antiferromagnetic order in Nd_2AgIn_3, Appl. Phys. Lett. **79**, 4183 (2002).
[10] P. Arora, M. K. Chattopadhyay, L. S. Sharath Chandra, V. K. Sharma, and S. B. Roy, Multiple magnetic transitions in Ag-substituted $DyPt_2$, J. Appl. Phys. **112**, 033906 (2012).
[11] D. K. Singh, A. Thamizhavel, J. W. Lynn, S. K. Dhar, and T. Hermann, Multiple magnetic structures of correlated Ce ions in intermetallic $CeAu_2Ge_2$, Phys. Rev. B **86**, 060405(R) (2012).
[12] S. Sarkar, M. J. Gutmann, and S. C. Peter, Crystal structure and magnetic properties of indium flux grown $EuAu_2In_4$ and $EuAuIn_4$, Cryst. Growth Des. **13**, 4285 (2013).
[13] S. Sarkar and S. C. Peter, Structural phase transitions in a new compound Eu_2AgGe_3, Inorg. Chem. **52**, 9741 (2013).
[14] K. Kaneko, T. Kawasaki, A. Nakamura, K. Munakata, A. Nakao, T. Hanashima, R. Kiyanagi, T. Ohhara, M. Hedo, T. Nakama *et al.*, Charge-density-wave order and multiple magnetic transitions in divalent europium compound $EuAl_4$, J. Phys. Soc. Japan **90**, 064704 (2021).
[15] N. Hanasaki, Y. Nogami, M. Kakinuma, S. Shimomura, M. Kosaka, and H. Onodera, Magnetic field switching of the charge-density-wave state in the lanthanide intermetallic $SmNiC_2$, Phys. Rev. B **85**, 092402 (2012).
[16] S. Ramakrishnan, S. R. Kotla, T. Rekis, J.-K. Bao, C. Eisele, L. Noohinejad, M. Tolkiehn, C. Paulmann, B. Singh, R. Verma *et al.*, Orthorhombic charge density wave on the tetragonal lattice of $EuAl_4$, IUCrJ **9**, 378 (2022).
[17] M. Stavinoha, J. A. Cooley, S. G. Minasian, T. M. McQueen, S. M. Kauzlarich, C. L. Huang, and E. Morosan, Charge density wave behavior and order-disorder in the antiferromagnetic metallic series $Eu(Ga_{1-x}Al_x)_4$, Phys. Rev. B **97**, 195146 (2018).
[18] A. Nakamura, Y. Hiranaka, M. Hedo, T. Nakama, Y. Miura, H. Tsutsumi, A. Mori, K. Ishida, K. Mitamura, Y. Hirose *et al.*, Unique Fermi surface and emergence of charge density wave in $EuGa_4$ and $EuAl_4$, JPS Conf. Proc. **3**, 011012 (2014).
[19] J. A. W. Straquadine, F. Weber, S. Rosenkranz, A. H. Said, and I. R. Fisher, Suppression of charge density wave order by disorder in Pd-intercalated $ErTe_3$, Phys. Rev. B **99**, 235138 (2019).
[20] S. M. Dubiel, K. H. Fischer, C. Sauer, and W. Zinn, Influence of an external magnetic field on the reentrant spin-glass transition temperature in a $Cr_{75}Fe_{25}$ alloy, Phys. Rev. B **36**, 360 (1987).
[21] S. Chatterjee, S. Giri, S. K. De, and S. Majumdar, Reentrant-spin-glass state in $Ni_2Mn_{1.36}Sn_{0.64}$ shape-memory alloy, Phys. Rev. B **79**, 092410 (2009).

[22] H. Maletta, G. Aeppli, and S. M. Shapiro, Spin correlations near the ferromagnetic-spin glass crossover in $Eu_xSr_{1-x}S$, J. Magn. Magn. Mater. **31–34**, 1367 (1983).

[23] D. Sherrington and S. Kirkpatrick, Solvable Model of a Spin-Glass, Phys. Rev. Lett. **35**, 1792 (1975).

[24] U. Subbarao and S. C. Peter, Crystal growth and properties of $YbCuGa_3$: first monoclinic system in the $RETX_3$ family, Cryst. Growth Des. **13**, 953 (2013).

[25] A. Kumar Singh, S. Sarkar, and S. C. Peter, Diversity in crystal structure and physical properties of $RETX_3$ (*RE*—rare earth, *T*—transition metal, *X*—main group element) intermetallics, Chem. Rec. **22**, e202100317 (2022).

[26] B. K. Rai, P. O'Rourke, and U. N. Roy, Review on crystal structures and magnetic properties of RTX_3 materials, J. Phys. Condens. Matter **34**, 273002 (2022).

[27] S. D. Ramarao, A. K. Singh, U. Subbarao, and S. C. Peter, An overview on the structural diversity of europium based ternary intermetallics, J. Solid State Chem. **281**, 121048 (2020).

[28] V. K. Anand, D. T. Adroja, and A. D. Hillier, Ferromagnetic cluster spin-glass behavior in $PrRhSn_3$, Phys. Rev. B **85**, 014418 (2012).

[29] V. K. Anand, D. T. Adroja, A. D. Hillier, J. Taylor, and G. André, Signatures of spin-glass behavior in the induced magnetic moment system $PrRuSi_3$, Phys. Rev. B **84**, 064440 (2011).

[30] R. Nagalakshmi, R. Kulkarni, S. K. Dhar, A. Thamizhavel, V. Krishnakumar, M. Reiffers, I. Čurlík, H. Hagemann, D. Lovy, and S. Nallamuthu, Magnetic properties of the tetragonal $RCuGa_3$ (R = Pr, Nd and Gd) single crystals, J. Magn. Magn. Mater. **386**, 37 (2015).

[31] K. Ghosh, S. Ramakrishnan, S. K. Dhar, S. K. Malik, G. Chandra, V. K. Pecharsky, K. A. Gschneidner, Z. Hu, and W. B. Yelon, Crystal structures and low-temperature behaviors of the heavy-fermion compounds $CeRuGe_3$ and Ce_3Ru_4Ge containing both trivalent and tetravalent cerium, Phys. Rev. B **52**, 7267 (1995).

[32] O. Bednarchuk, A. Gągor, and D. Kaczorowski, Synthesis, crystal structure and physical properties of $EuTGe_3$ (T = Co, Ni, Rh, Pd, Ir, Pt) single crystals, J. Alloys Compd. **622**, 432 (2015).

[33] R. J. Goetsch, V. K. Anand, and D. C. Johnston, Antiferromagnetism in $EuNiGe_3$, Phys. Rev. B **87**, 064406 (2013).

[34] X. Fabrèges, A. Gukasov, P. Bonville, A. Maurya, A. Thamizhavel, and S. K. Dhar, Exploring metamagnetism of single crystalline $EuNiGe_3$ by neutron scattering, Phys. Rev. B **93**, 214414 (2016).

[35] A. Maurya, P. Bonville, A. Thamizhavel, and S. K. Dhar, $EuNiGe_3$, an anisotropic antiferromagnet, J. Phys. Condens. Matter **26**, 216001 (2014).

[36] S. Bobev, E. D. Bauer, J. D. Thompson, and J. L. Sarrao, Single crystal growth, and magnetic and electronic properties of $EuGa_4$, J. Magn. Magn. Mater. **277**, 236 (2004).

[37] H. Zhang, X. Y. Zhu, Y. Xu, D. J. Gawryluk, W. Xie, S. L. Ju, M. Shi, T. Shiroka, Q. F. Zhan, E. Pomjakushina *et al.*, Giant magnetoresistance and topological Hall effect in the $EuGa_4$ antiferromagnet, J. Phys. Condens. Matter **34**, 034005 (2022).

[38] T. Shang, Y. Xu, D. J. Gawryluk, J. Z. Ma, T. Shiroka, M. Shi, and E. Pomjakushina, Anomalous Hall resistivity and possible topological Hall effect in the $EuAl_4$ antiferromagnet, Phys. Rev. B **103**, L020405 (2021).

[39] A. Nakamura, T. Uejo, F. Honda, T. Takeuchi, H. Harima, E. Yamamoto, Y. Haga, K. Matsubayashi, Y. Uwatoko, M. Hedo *et al.*, Transport and magnetic properties of $EuAl_4$ and $EuGa_4$, J. Phys. Soc. Japan **84**, 124711 (2015).

[40] X. Y. Zhu, H. Zhang, D. J. Gawryluk, Z. X. Zhen, B. C. Yu, S. L. Ju, W. Xie, D. M. Jiang, W. J. Cheng, Y. Xu *et al.*, Spin order and fluctuations in the $EuAl_4$ and $EuGa_4$ topological antiferromagnets: A μSR study, Phys. Rev. B **105**, 014423 (2022).

[41] T. Kawasaki, K. Kaneko, A. Nakamura, N. Aso, M. Hedo, T. Nakama, T. Ohhara, R. Kiyanagi, K. Oikawa, I. Tamura *et al.*, Magnetic structure of divalent europium compound $EuGa_4$ studied by single-crystal time-of-flight neutron diffraction, J. Phys. Soc. Japan **85**, 114711 (2016).

[42] G. D. Loula, R. D. dos Reis, D. Haskel, F. Garcia, N. M. Souza-Neto, and F. C. G. Gandra, High-pressure tuning of valence and magnetic interactions in $Eu_{0.5}Yb_{0.5}Ga_4$, Phys. Rev. B **85**, 245128 (2012).

[43] A. K. Iyer, L. Balisetty, S. Sarkar, and S. C. Peter, Effect of Li and Mg substitution on the crystal structure and magnetism of the $REGa_2$ (RE = Ce and Eu) and $EuGa_4$ compounds, J. Alloys Compd. **582**, 305 (2014).

[44] P. H. Tobash and S. Bobev, Synthesis, flux crystal growth, structure and properties of the new rare-earth compounds $Eu\,Al_{4-x}Si_x$($x \sim 1$), TmAlSi and LuAlSi, J. Alloys Compd. **418**, 58 (2006).

[45] G. M. Sheldrick, Crystal structure refinement with SHELXL, Acta Cryst. C **71**, 3 (2014).

[46] See Supplemental Material at http://link.aps.org/supplemental/10.1103/PhysRevB.106.224414 for experimental results from SCXRD, TIRM fitting and Magnetic structure energy tables.

[47] P. Giannozzi, S. Baroni, N. Bonini, M. Calandra, R. Car, C. Cavazzoni, D. Ceresoli, G. L. Chiarotti, M. Cococcioni, I. Dabo *et al.*, QUANTUM ESPRESSO: A modular and open-source software project for quantum simulations of materials, J. Phys. Condens. Matter **21**, 395502 (2009).

[48] J. P. Perdew, K. Burke, and M. Ernzerhof, Generalized Gradient Approximation Made Simple, Phys. Rev. Lett. **77**, 3865 (1996).

[49] P. E. Blöchl, Projector augmented-wave method, Phys. Rev. B **50**, 17953 (1994).

[50] A. Fedorchuk, Y. Prots, and Y. Grin, Crystal structures of europium magnesium gallium, $EuMg_xGa_{4-x}$, and europium lithium gallium, $EuLi_xGa_{4-x}$(x 0.5), Z. Krist. New Cryst. Struct. **220**, 337 (2005).

[51] T.-S. You and G. J. Miller, Phase width and site preferences in the $EuMg_xGa_{4-x}$ series, Z. anorg. allg. Chem. **634**, 2845 (2008).

[52] U. Häussermann, S. Amerioun, L. Eriksson, C.-S. Lee, and G. J. Miller, The *s-p* bonded representatives of the prominent $BaAl_4$ structure type: A case study on structural stability of polar intermetallic network structures, J. Am. Chem. Soc. **124**, 4371 (2002).

[53] X.-F. Gu, T. Furuhara, and W.-Z. Zhang, PTCLab: Free and open-source software for calculating phase transformation crystallography, J. Appl. Crystallogr. **49**, 1099 (2016).

[54] E. V. Sampathkumaran, L. C. Gupta, R. Vijayaraghavan, K. V. Gopalakrishnan, R. G. Pillay, and H. G. Devare, A new and unique Eu-based mixed valence system: $EuPd_2Si_2$, J. Phys. C Solid State Phys. **14**, L237 (1981).

[55] U. Subbarao and S. C. Peter, Crystal structure of $YbCu_6In_6$ and mixed valence behavior of Yb in $YbCu_{6-x}In_{6+x}$(x = 0, 1, and 2) solid solution, Inorg. Chem. **51**, 6326 (2012).

[56] G. D. Loula, L. M. da Silva, A. O. dos Santos, A. N. Medina, and F. G. Gandra, Evidence of mixed valence in $(Eu_{1-x}Yb_x)Ga_4$ single crystals, Phys. B Condens. Matter **403**, 946 (2008).

[57] M. Chondroudi, S. C. Peter, C. D. Malliakas, M. Balasubramanian, Q. Li, and M. G. Kanatzidis, Yb_3AuGe_2In: An ordered variant of the YbAuIn structure exhibiting mixed-valent Yb behavior, Inorg. Chem. **50**, 1184 (2011).

[58] A. P. Ramirez, Strongly geometrically frustrated magnets, Annu. Rev. Mater. Sci. **24**, 453 (1994).

[59] S. Ghara, B. G. Jeon, K. Yoo, K. H. Kim, and A. Sundaresan, Reentrant spin-glass state and magnetodielectric effect in the spiral magnet $BiMnFe_2O_6$, Phys. Rev. B **90**, 024413 (2014).

[60] J. R. L. de Almeida and D. J. Thouless, Stability of the Sherrington-Kirkpatrick solution of a spin glass model, J. Phys. A. Math. Gen. **11**, 983 (1978).

[61] R. C. B. and S. B. Roy, *Re-Entrant Spin-Glasses: Do They Exist?* (World Scientific, Singapore, 1993).

[62] S. M. Thomas, P. F. S. Rosa, S. B. Lee, S. A. Parameswaran, Z. Fisk, and J. Xia, Hall effect anomaly and low-temperature metamagnetism in the Kondo compound $CeAgBi_2$, Phys. Rev. B **93**, 075149 (2016).

[63] A. Baumgartner, D. Neubauer, S. Zapf, A. V. Pronin, W. H. Jiao, G. H. Cao, and M. Dressel, Reentrant phases in electron-doped $EuFe_2As_2$: Spin glass and superconductivity, Phys. Rev. B **95**, 174522 (2017).

[64] A. Malinowski, V. L. Bezusyy, R. Minikayev, P. Dziawa, Y. Syryanyy, and M. Sawicki, Spin-glass behavior in Ni-doped $La_{1.85}Sr_{0.15}CuO_4$, Phys. Rev. B **84**, 024409 (2011).

[65] W. Kinzel, Remanent magnetization in spin-glasses, Phys. Rev. B **19**, 4595 (1979).

[66] S. Dhar, O. Brandt, A. Trampert, K. J. Friedland, Y. J. Sun, and K. H. Ploog, Observation of spin-glass behavior in homogeneous (Ga,Mn)N layers grown by reactive molecular-beam epitaxy, Phys. Rev. B **67**, 165205 (2003).

[67] E. L. Thomas, D. P. Gautreaux, and J. Y. Chan, The layered intermetallic compound $LaPdSb_3$, Acta Cryst. E **62**, i96 (2006).

[68] F. Casper, C. Felser, R. Seshadri, C. Peter Sebastian, and R. Pöttgen, Searching for hexagonal analogues of the half-metallic half-Heusler XYZ compounds, J. Phys. D. Appl. Phys. **41**, 035002 (2008).

[69] M. Ulrich, J. García-Otero, J. Rivas, and A. Bunde, Slow relaxation in ferromagnetic nanoparticles: Indication of spin-glass behavior, Phys. Rev. B **67**, 024416 (2003).

[70] S. H. Chun, Y. Lyanda-Geller, M. B. Salamon, R. Suryanarayanan, G. Dhalenne, and A. Revcolevschi, Reentrant spin glass behavior in layered manganite $La_{1.2}Sr_{1.8}Mn_2O_7$ single crystals, J. Appl. Phys. **90**, 6307 (2001).

[71] J. A. Mydosh, *Spin Glasses: An Experimental Introduction* (CRC Press, London, 1993).

[72] A. K. Nayak, M. Nicklas, S. Chadov, C. Shekhar, Y. Skourski, J. Winterlik, and C. Felser, Large Zero-Field Cooled Exchange-Bias in Bulk Mn_2PtGa, Phys. Rev. Lett **110**, 127204 (2013).

[73] J. Yin, C. Wu, L. Li, J. Yu, H. Sun, B. Shen, B. A. Frandsen, D.-X. Yao, and M. Wang, Large negative magnetoresistance in the antiferromagnetic rare-earth dichalcogenide $EuTe_2$, Phys. Rev. Mater. **4**, 013405 (2020).

[74] M. Bartolozzi, T. Surungan, D. B. Leinweber, and A. G. Williams, Spin-glass behavior of the antiferromagnetic Ising model on a scale-free network, Phys. Rev. B **73**, 224419 (2006).

[75] C. P. Herrero, Antiferromagnetic Ising model in small-world networks, Phys. Rev. E **77**, 041102 (2008).